Surface & Coatings Technology 433 (2022) 128091

Contents lists available at ScienceDirect

Surface & Coatings Technology

journal homepage: www.elsevier.com/locate/surfcoat

The influence of WS_2 layer thickness on microstructures and mechanical behavior of high-entropy (AlCrTiZrNb)N/WS_2 nanomultilayered films

Panpan Cui [a], Wei Li [a,*], Ping Liu [a], Jingjing Wang [a], Xun Ma [a], Ke Zhang [a], Fengcang Ma [a], Xiaohong Chen [a], Rui Feng [b], Peter K. Liaw [c]

[a] School of Materials and Chemistry, University of Shanghai for Science and Technology, Shanghai 200093, China
[b] Neutron Scattering Division, Oak Ridge National Laboratory, Oak Ridge, TN 37831, USA
[c] Department of Materials Science and Engineering, The University of Tennessee, Knoxville, TN 37996, USA

ARTICLE INFO

Keywords:
High-entropy (AlCrTiZrNb)N/WS_2 nano-multilayered film
Microstructure
Mechanical properties

ABSTRACT

High-entropy (AlCrTiZrNb)N/WS_2 nano-multilayers with different thicknesses of WS_2 layers were synthesized by reactive magnetron sputtering. The influence of MoS_2 layers on the microstructure of the nano-multilayered films was studied by X-ray diffraction (XRD), scanning electron microscope (SEM), and high-resolution transmission electron microscope (HRTEM). Mechanical properties were examined through nanoindentation, HSR-2M coating friction and wear tester. The results show that when the thickness of the WS_2 layer is less than 1.2 nm, the WS_2 layer can be transformed into a cubic phase under the action of the (AlCrTiZrNb)N layer template, and a coherent epitaxial interface layer is formed between the two layers, resulting in an increase in hardness. The maximum values of hardness and elastic modulus of the high-entropy (AlCrTiZrNb)N/WS_2 film are 22.5 GPa and 300.6 GPa, respectively, when the WS_2 layer thickness reaches 1.2 nm. As the thickness of the WS_2 layer further increases, the WS_2 layer cannot maintain the cubic structure and the epitaxial growth interface is destroyed, resulting in a decrease in the hardness. The friction coefficient of the (AlCrTiZrNb)N/WS_2 nano-multilayered film is lower than that of the (AlCrTiZrNb)N monolithic film.

1. Introduction

Compared with traditional alloys, high-entropy alloys (HEAs) have many excellent properties, which attract the attention of many researchers. For example, a large number of studies show that HEAs have high strength [1], high hardness [2,3], wear resistance [4–6], fatigue resistance [7–11], and corrosion resistance [12–16]. The so-called HEA is a concept proposed by Professor Yeh in 2004 [17–20]. The HEA is composed of five or more kinds of metal or nonmetal elements in an equimolar or near-molar ratio, with content of each element ranging from 5% to 35% [21–23]. Similarly, Cantor et al. [24] has reported the concept of multi-principal element alloys. It is generally believed that with the increase of the number of alloying elements, complex phases and intermetallic compounds tend to form in the alloy, which leads to the decrease of mechanical properties. During the solidification of HEAs, due to the high-entropy effect, the HEA not only does not form intermetallic compounds after solidification, but present a simple face-centered-cubic (FCC), body-centered-cubic (BCC), or hexagonal-close-packed (HCP) crystalline phase [25–27], or two phases in common alloys, such as eutectic high-entropy alloys (EHEAs) [28–30].

It is well known that the nitrides of transition metals have excellent mechanical properties. The selected elements in HEAs are mainly transition metals, such as Al, Cr, Ti, and Zr. These elements are also strong nitride forming elements, which can combine with N elements to form nitride films with better mechanical properties. Hsieh et al. [31] reported the (AlCrNbSiTiV)N HEA nitride film prepared by a direct current (DC) reactive magnetron sputtering method and studied the microstructures, mechanical properties and tribological properties. Their experimental results indicated that the high-entropy (AlCrNbSiTiV)N film presented a simple FCC structure and significantly enhanced the mechanical properties with the improvement in friction coefficient of 32.5% and in hardness of 29.4%.

In 1970, Koehler [32] proposed the concept of a nano-multilayered film, which is a nanometer-thick multilayer film formed by depositing two or more materials alternately. Compared with single-layer films, nano-multilayers often exhibit the superhard phenomenon with greatly

* Corresponding author at: School of Materials and Chemistry, University of Shanghai for Science and Technology, Shanghai 200093, China.
E-mail address: liwei176@usst.edu.cn (W. Li).

https://doi.org/10.1016/j.surfcoat.2022.128091
Received 16 December 2020; Received in revised form 29 December 2021; Accepted 4 January 2022
Available online 12 January 2022

improved hardness due to the "template effect", which to some extent solves the situation that coating materials are more and more demanding in the industrial development. Zhang et al. [33] prepared TiN/Mo_2N nano-multilayers by magnetron sputtering and found that the nano-multilayers showed (200) preferential orientation, and an FCC structure similar to B1-NaCl, with the superhardness about 41 GPa. Compared with TiN and Mo_2N single-layer films, the mechanical and tribological properties of TiN/Mo_2N nano-multilayered films had been greatly improved.

In recent years, due to the excellent properties, the HEA nitride thin film and nano-multilayered film have attracted more and more attention of researchers. However, the research on nano-multilayered films included HEA nitride has been rarely documented. To this end, in this study, HEA nitride (AlCrTiZrNb)N and WS_2 were designed and selected as the template layer and the modulation layer within the nano-multilayered film, respectively, and the high-entropy (AlCrTiZrNb)N/WS_2 nano-multilayered film was synthesized. Since WS_2 is an excellent solid-lubricating material, the synthesized (AlCrTiZrNb)N/WS_2 nano-multilayered film is expected to have both good mechanical properties and great wear resistance for the industrial application.

2. Experimental

2.1. Film preparation

In the JGP-450 multi-target magnetron sputtering system, the high-entropy AlCrTiZrNb HEA target with a purity of at least 99.99% (mass fraction) and WS_2 target with a purity of at least 99.99% (weight percent) were used. In pure Ar atmosphere, an (AlCrTiZrNb)N layer was deposited from the AlCrTiZrNb HEA target using a DC mode with a power setting of 180 W. The WS_2 layer was sputtered from the WS_2 target in the RF mode with the power set of 100 W. The thin film is deposited on a single crystal silicon wafer with the size of 30 mm × 20 mm × 1 mm. The silicon wafer is cleaned before deposition. First, the silicon wafer was immersed in ethanol, and then placed in an ultrasonic cleaning chamber for 15 min. The silicon wafer is dried and placed in a vacuum chamber for reverse sputtering cleaning. When the working pressure is 0.5 Pa, the flow rates of N_2 and Ar are both 15 standard cubic centimeter per minute (sccm). By controlling the deposition time of the WS_2 layer, the (AlCrTiZrNb)N/WS_2 nano-multilayered films with thicknesses of 0, 0.2 nm, 0.4 nm, 0.6 nm, 0.8 nm, 1.0 nm, 1.2 nm, and 1.4 nm were prepared. During the deposition process, the silicon wafer was not heated and no bias potential was used. The distance between target and substrate were set as 6 cm.

2.2. Film characterization and measurement

The phase composition of high-entropy (AlCrTiZrNb)N/WS_2 nano-multilayers were analyzed by the D8 Advance X-ray diffractometer (XRD, Bruker, Germany) using the CuK_α radiation (λ = 0.15406 nm) with a measurement range from 20° to 90°. The microstructures of the films were observed by the Quanta FEG450 field emission environmental electron microscope (FESEM, FEI, USA) and Tecnai $G^2$20 high-resolution field-emission transmission electron microscope (HRTEM, FEI, USA). The hardness of the film was measured by a NANO Indenter G200 nanoindenter (Agilent, USA) with the Berkovich indenter. The load-unload curve was obtained by accurately recording the change of the indentation depth with load. The hardness of the material was calculated by the Oliver-Pharr model [34]. The depth of penetration was less than 1/10 of the film thickness in order to eliminate the effect of the substrate on the hardness of the film. The friction coefficient of the film was measured by the HRS-2 M high-speed friction and wear tester. The friction pair was a GCr15 steel ball with a diameter of 4 mm. The applied load was 8 N and the test time was 5 min.

3. Results

3.1. Microstructures

Fig. 1 shows the XRD patterns of (AlCrTiZrNb)N/WS_2 nano-multilayers with different WS_2 thicknesses. The thickness of the WS_2 layer in each sample has been marked in the figure. It can be seen from the figure that the (AlCrTiZrNb)N thin film and the (AlCrTiZrNb)N/WS_2 nano-multilayered films both have an FCC structure. The high-entropy (AlCrTiZrNb)N/WS_2 nano-multilayered films exhibit (111) and (200) preferred orientations. As the thickness of the WS_2 layer increases, the (111) and (200) peaks of the (AlCrTiZrNb)N/WS_2 nano-multilayers first become large and then small. When the thickness of the WS_2 layer is 1.2 nm, the peak intensity reaches the maximum value. Based on the previous research, when the thickness of the WS_2 layer is less than 1.2 nm, under the action of the (AlCrTiZrNb)N template, the WS_2 layer and (AlCrTiZrNb)N form a co-epitaxial growth structure. Therefore, the crystallinity of the thin film increases, and accordingly, the intensity of its diffraction peak increases. When the thickness of the WS_2 layer is greater than 1.2 nm, the coextensive epitaxial growth of the WS_2 layer and (AlCrTiZrNb)N is destroyed. Hence, the crystallinity of the nano-multilayered film is reduced, and the diffraction peak intensity of the film becomes weak.

Fig. 2 is the HRTEM images of the cross-sectional morphology of the (AlCrTiZrNb)N monolithic film and the (AlCrTiZrNb)N/WS_2 nano-multilayered film with the WS_2 layer thickness of 1.2 nm. As can be seen from the low-magnification image of Fig. 2(a), the nano-multilayered film has a well-defined layer structure, and the interface is smooth and clear. In addition, the high-entropy (AlCrTiZrNb)N/WS_2 nano-multilayered film has a good columnar structure along the growth direction of the film. The columnar structure continues through several modulation cycles of the nano-multilayered film, which also proves that the insertion of the WS_2 layer does not damage the growth of the columnar crystal. The diffraction rings of (111) and (200) FCC structures appear in the inserted selected area electron diffraction (SAED) diagram, which is consistent with the results in the XRD patterns. Fig. 2(b) is a moderately-enlarged cross-sectional morphology, from which we can see a well-grown nano-multilayered film structure. According to the contrast, the bright and dark stripes correspond to the (AlCrTiZrNb)N and WS_2 layers, respectively. The (AlCrTiZrNb)N and WS_2 layers are alternately deposited to form a continuous nano-multilayered film structure. Fig. 2(c) is a high magnification HRTEM image in the selected area of Fig. 2(b). The lattice fringes can pass through several modulation cycles continuously, indicating that the WS_2 layer is transformed into an

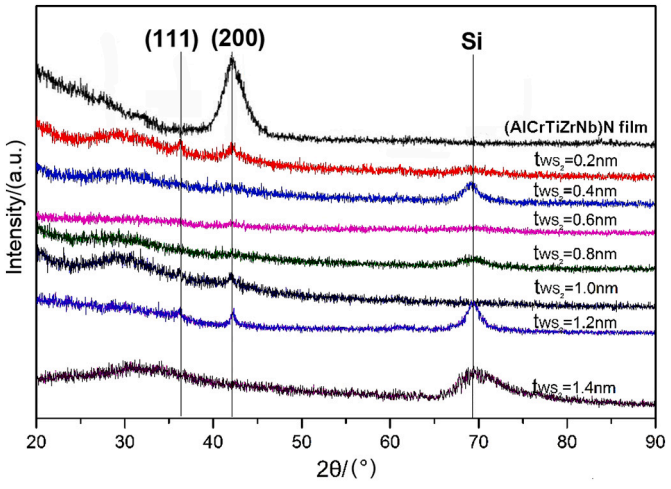

Fig. 1. XRD patterns of (AlCrTiZrNb)N/WS_2 nano-multilayered films with different WS_2 thickness.

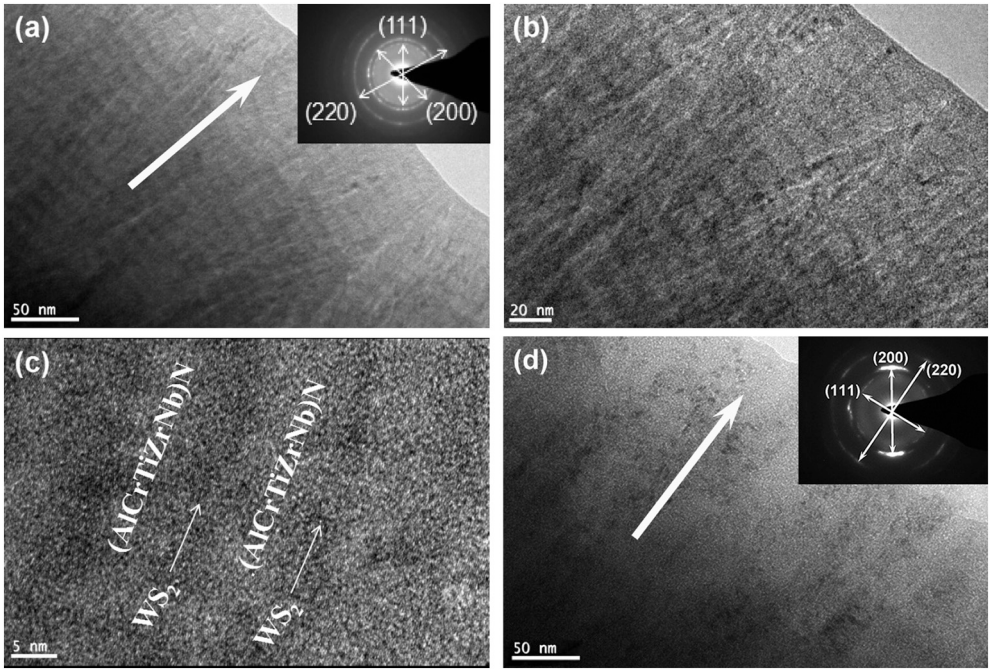

Fig. 2. Cross-sectional HRTEM images of the (AlCrTiZrNb)N monolithic film and (AlCrTiZrNb)N/WS_2 nano-multilayered film with the WS_2 layer thickness of 1.2 nm: (a) low-magnification, (b) medium-magnification, (c) high-magnification of (AlCrTiZrNb)N/WS_2 nano-multilayered film and (d) low-magnification of (AlCrTiZrNb)N monolithic film. (The insertions in (a) and (d) are their corresponding selected area diffraction patterns.)

FCC structure under the "template effect" of the (AlCrTiZrNb)N layer, and co-epitaxially grown with the high-entropy (AlCrTiZrNb)N layer. Fig. 2(d) displays the cross-sectional HRTEM observation of (AlCrTiZrNb)N monolithic film, which exhibits a typical columnar crystal structure with the growth direction marked by the arrow. The inserted SAED patterns indicate that the (AlCrTiZrNb)N film exbihits the FCC structure with the (200) preferred orientation.

Fig. 3 shows the cross-sectional SEM morphology of nano-multilayered films with different WS_2 layer thicknesses. In Fig. 3(a), the (AlCrTiZrNb)N film shows a columnar growth structure. In Fig. 3(b), (c) and (d), the (AlCrTiZrNb)N/WS_2 film also presents a similar columnar growth structure, which indicates that under the "template effect", the WS_2 and high-entropy (AlCrTiZrNb)N layers grow epitaxially together when the WS_2 thickness is less than 1.2 nm. In Fig. 3(e), when the thickness of WS_2 is 1.4 nm, the columnar crystal structure of the nano-multilayered film is less obvious than before, indicating that

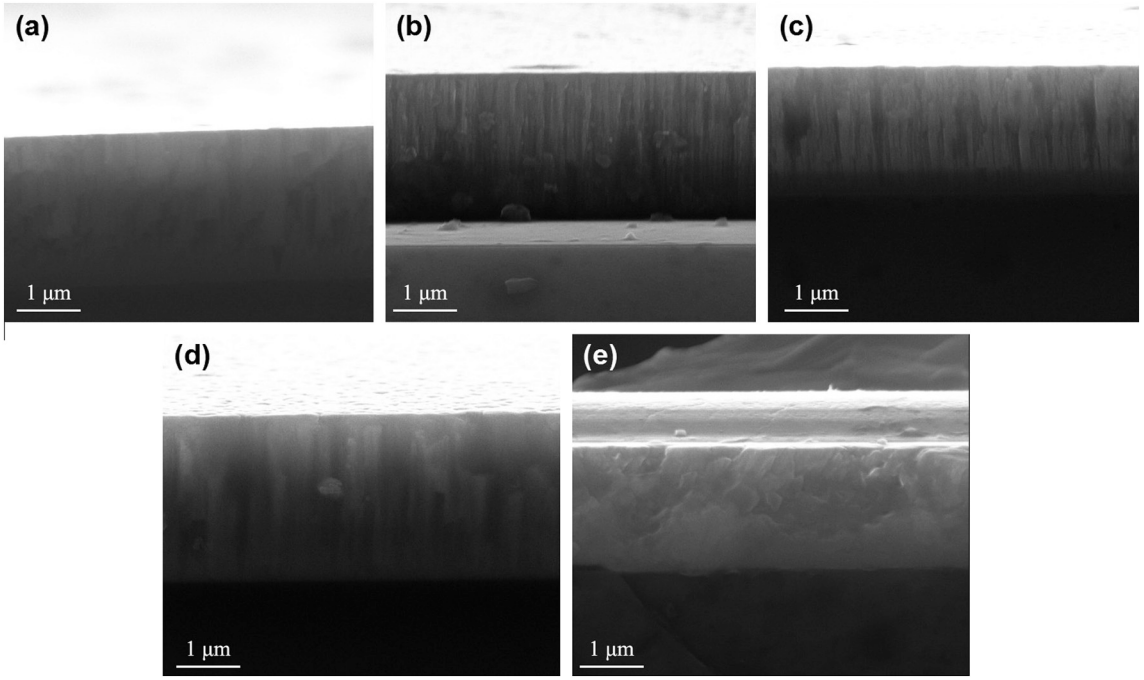

Fig. 3. Cross-sectional SEM images of nano-multilayered films with different WS_2 thicknesses: (a) $tws_2 = 0$, (b) $tws_2 = 0.4$ nm, (c) $tws_2 = 0.8$ nm, (d) $tws_2 = 1.2$ nm, and (e) $tws_2 = 1.4$ nm.

the growth structure of the nano-multilayered film is damaged, and the FCC structure cannot be maintained, which is consistent with the results in XRD.

3.2. Mechanical properties

Fig. 4 shows the hardness and elastic modulus of high-entropy (AlCrTiZrNb)N/WS_2 nano-multilayered films with different WS_2 layer thicknesses. It can be seen that the hardness and elastic modulus of the monolithic (AlCrTiZrNb)N film are 13.6 GPa and 211.2 GPa, respectively. As the thickness of the WS_2 layer increases, the hardness and elastic modulus of the nano-multilayered film show an upward trend. When the thickness of the WS_2 layer is 1.2 nm, the hardness and elastic modulus of the film reach the maximum of 22.5 GPa and 300.6 GPa, respectively. When the thickness of the WS_2 layer is less than 1.2 nm, the WS_2 layer is transformed into an FCC structure under the "template effect" of the (AlCrTiZrNb)N layer, and co-epitaxially grown together with the (AlCrTiZrNb)N layer. The hardness and elastic modulus of the high-entropy (AlCrTiZrNb)N/WS_2 film are both improved, compared to those of the (AlCrTiZrNb)N film. However, when the thickness of the WS_2 layer is greater than 1.2 nm, the coextensive epitaxial growth structure between the WS_2 and the (AlCrTiZrNb)N layer is destroyed, and the WS_2 layer is transformed into a hexagonal structure, resulting in the disappearance of the enhancement effect. Therefore, the hardness and elastic modulus of the nano-multilayered film are reduced.

Fig. 5 is the change of friction coefficients of (AlCrTiZrNb)N/WS_2 nano-multilayers with different WS_2 layer thicknesses. It can be seen that the friction coefficient of the (AlCrTiZrNb)N is 0.68. As the thickness of the WS_2 layer increases, the overall friction coefficient of the nano-multilayered film decreases first, then increases, and subsequently decreases, When the thickness of the WS_2 layer is 1.2 nm, the friction coefficient of the (AlCrTiZrNb)N/WS_2 nano-multilayered film is 0.41. In general, the friction coefficients of high-entropy (AlCrTiZrNb)N/WS_2 nano-multilayers are between 0.20 and 0.55, which are much smaller than that of the monolithic (AlCrTiZrNb)N film.

Fig. 6 displays SEM micrographs of the wear tracks on the (AlCrTiZrNb)N/WS_2 nano-multilayered films with different WS_2 layer thicknesses. As shown in Fig. 6(a), large flakes peel off on the wear track of the monolithic high-entropy (AlCrTiZrNb)N. In Fig. 6(b), it is seen that dense and continuous tribo-films are formed on the wear track for the nano-multilayered film with the WS_2 layer thickness of 0.8 nm. In Fig. 6 (c), for the nano-multilayered film with the WS_2 layer thickness of 1.2 nm, no obviously tribo-films are formed on the wear track. In Fig. 6(d), some little flakes of tribo-films appear on the wear track of (AlCrTiZrNb)N/WS_2 nano-multilayered films with the WS_2 layer thickness of 1.4 nm.

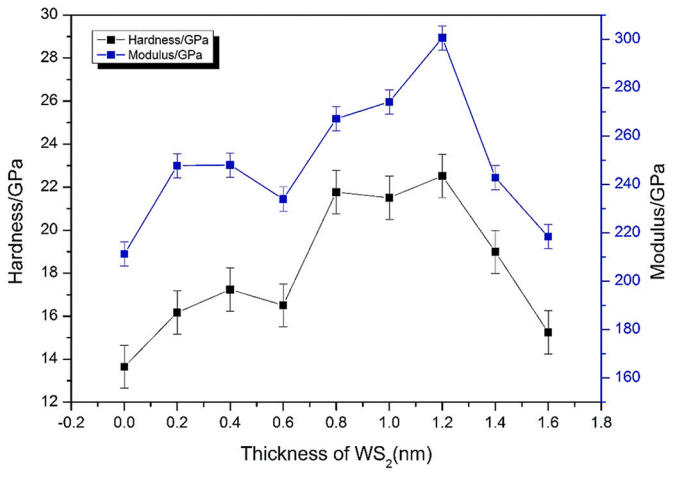

Fig. 4. Hardness and elastic modulus of the (AlCrTiZrNb)N/WS_2 nano-multilayered films with different WS_2 layer thicknesses.

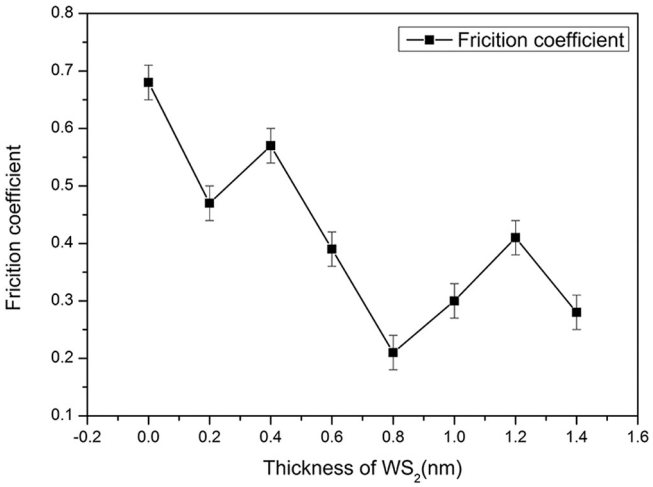

Fig. 5. Change of the friction coefficient of the (AlCrTiZrNb)N/WS_2 nano-multilayered films with different WS_2 layer thickness.

4. Discussion

4.1. Effect of the WS_2 layer thickness on microstructures of the high-entropy (AlCrTiZrNb)N/WS_2 nano-multilayered films

When the film grows in the atomic or molecular state on the substrate from the initial nucleation, the interface energy is the main part of the system energy, and the substrate surface has an important influence on the growth of the film. In the nano-multilayered film, the crystal structure of the firstly deposited layer can similarly have a significant effect on the crystal growth and structure of the later deposited layer. Therefore, the subsequently deposited layer forms a crystal structure that has a good interface match with the first deposited layer, which is called the "template effect". This phenomenon is consistent with the previous research on nano-multilayers, such as W/Mo [35], TiN/VN [36], TiN/NbVN [37], TiN/TaN [38], TiN/Nb [39], and TiN/$CrN_{0.6}$ [40]. Under the effect of the (AlCrTiZrNb)N template with a stable FCC structure, the WS_2 with the hexagonal structure can form a metastable phase and maintain a cubic structure when its thickness is less than 1.2 nm, leading to the fact of the (AlCrTiZrNb)N/WS_2 nano-multilayered film exhibits an FCC structure.

Through the SEM image of the high-entropy (AlCrTiZrNb)N/WS_2 nano-multilayered film, the columnar crystal structure at the fracture of the (AlCrTiZrNb)N/WS_2 nano-multilayered film can be clearly observed. According to the HRTEM image of the (AlCrTiZrNb)N/WS_2 nano-multilayered film, the nano-multilayered film has a well-defined layered structure. The interface is smooth and clear, and the columnar structure passes through several modulation periods of the nano-multilayered film. Combined with the selected area electron diffraction patterns, it can be confirmed that the (AlCrTiZrNb)N/WS_2 nano-multilayered film presents an FCC structure.

4.2. Effect of the WS_2 layer thickness on mechanical properties of the high-entropy (AlCrTiZrNb)N/WS_2 nano-multilayered film

The changes of hardness and elastic modulus are closely related to the microstructure of the nano-multilayered film. With the addition of WS_2, under the "template effect" of the (AlCrTiZrNb)N layer, the WS_2 layer is forced to transform into an FCC structure and grow epitaxially with the (AlCrTiZrNb)N layer. At the same time, the nano-multilayered film shows a super-hard effect. However, when the thickness of the WS_2 layer exceeds 1.2 nm, the WS_2 layer cannot maintain the FCC crystal structure and change back to the hexagonal structure, resulting in a decrease in hardness and elastic modulus.

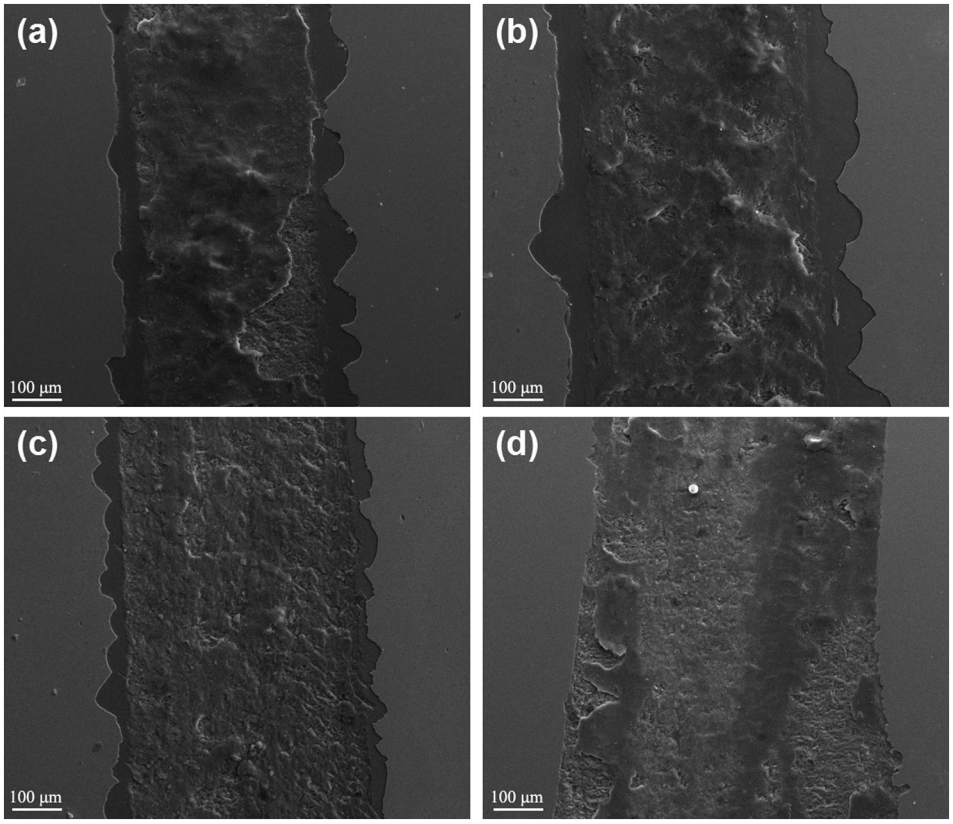

Fig. 6. SEM micrographs of the wear trajectories of the (AlCrTiZrNb)N/WS_2 nano-multilayered films with different WS_2 layer thicknesses: (a) $t_{WS2} = 0$, (b) $t_{WS2} = 0.8$ nm, (c) $t_{WS2} = 1.2$ nm, and (d) $t_{WS2} = 1.4$ nm.

The abnormal enhancement of hardness and elastic modulus can also be clarified by the Koehler's modulus-difference-strengthening theory [26] and Kato's alternating stress strengthening theory [41]. According to Koehler's theory [26], due to the different shear modulus, forces are generated from the (AlCrTiZrNb)N and WS_2 layers. Therefore, when dislocations traverse the interface of the nano-multilayered film, they will be hindered by the force generated from two materials with different shear moduli. In nano-multilayered films, the greater the difference between the shear moduli of the two layers, the more the additional stress can prevent the dislocation movement. The shear modulus (G) can be expressed as:

$$G = \frac{E}{2(1+\nu)} \tag{1}$$

where E is the elastic modulus, and ν is the Poisson's ratio. According to the experimental results: $E_{(AlCrTiZrNb)N} = 211.2$ GPa, $E_{WS2} = 90$ GPa, and $\nu = 0.25$. Combined with the formula, the shear modulus of (AlCrTiZrNb)N and WS_2 can be calculated as $G_{(AlCrTiZrNb)N} = 84.5$ GPa and $G_{WS2} = 36$ GPa respectively. The experimental results show that the increase in the hardness and elastic modulus in the nano-multilayered film can be explained by the enhancement effect caused by the difference in shear moduli.

Moreover, from the XRD patterns, it can be seen that, compared with the (AlCrTiZrNb)N monolithic film, most of the nano-multilayered films show a deviation to a small angle in the (200) and (111) diffraction peaks, which indicates that along the growth direction, alternating compressive stress and tensile stress fields are generated on the nano-multilayered film. According to Kato's theory [41], alternating compressive and tensile stress fields can also hinder dislocation motion and enhance the nano-multilayered film. Therefore, when the thickness of the WS_2 layer is less than 1.2 nm, the WS_2 layer is converted into an FCC crystal structure and epitaxially grown together with the (AlCrTiZrNb)N layer. The interface stress between the (AlCrTiZrNb)N and WS_2 layer is relatively low. As the thickness of the WS_2 layer increases, when the thickness of the WS_2 exceeds 1.2 nm, the epitaxial growth structures of the WS_2 and (AlCrTiZrNb)N layer are destroyed, the interface stress increases, and the dislocation motion cannot be prevented at the interface. As a result, the hardness and elastic modulus of the nano-multilayered film decrease.

For the friction coefficient of the high-entropy (AlCrTiZrNb)N/WS_2 nano-multilayered film, since WS_2 presents the superior lubrication property, the friction coefficient is significantly reduced with the addition of WS_2 layer. As the thickness of the WS_2 layer increases, the friction coefficient of (AlCrTiZrNb)N/WS_2 nano-multilayered film decreases in addition to the film with the WS_2 layer thickness of 0.4 nm. When the thickness of the WS_2 layer is 0.8 nm, the friction coefficient reaches a minimum value, which is also attributed to the formation of continuous tribo-films as seen in the Fig. 6(b). When the thickness of the WS_2 layer increases to 1.2 nm, the friction coefficient increases, which could be due to the two reasons as follows. Firstly, it is because that there is no obvious tribo-films formed on the wear track. Secondly, the best epitaxial growth is present as the thickness of the WS_2 layer is 1.2 nm, which means that the hexagonal structure of WS_2 layer significantly transform into an FCC structure under the “template effect” of the high-entropy (AlCrTiZrNb)N layer as proved by the XRD results. Therein, the hexagonal layered structure closely related to lubrication performance of WS_2 is greatly destroyed, thus leading to the higher friction. However, when the thickness of the WS_2 layer increases to 1.4 nm, the friction coefficient behaves a decreased trend. It is attributed to the formation of tribo-film, as well as the destruction of the epitaxial growth structure, making the WS_2 layer changing back into the original hexagonal structure state.

5. Conclusions

A series of high-entropy (AlCrTiZrNb)N/WS_2 nano-multilayered films with different WS_2 layer thicknesses were synthesized by reactive magnetron sputtering. The effects of inserting nano-layers of WS_2 with different thicknesses on the microstructures and mechanical properties of (AlCrTiZrNb)N/WS_2 were studied. The conclusions are drawn as follows:

(1) The high-entropy (AlCrTiZrNb)N/WS_2 nano-multilayered film exhibits an FCC structure. When the thickness of the WS_2 layer is less than 1.2 nm, the WS_2 layer is transformed into a cubic structure and coextensively grown with the (AlCrTiZrNb)N layer. When the thickness of the WS_2 layer exceeds 1.2 nm, the WS_2 layer of the FCC structure changes back to the hexagonal structure, leading to the destruction of the FCC structure within the (AlCrTiZrNb)N/WS_2 nano-multilayered film.

(2) When the thickness of WS_2 film increases, the mechanical properties of the nano-multilayers first increase and then decrease. The maximal hardness and elastic modulus are 22.5 GPa and 300.6 GPa, respectively, when the WS_2 film thickness is 1.2 nm. The enhancement effect can be explained by the difference in the shear modulus and the formation of alternating stress fields.

(3) The friction coefficients of (AlCrTiZrNb)N/WS_2 nano-multilayers are in the range of 0.20 to 0.55. As the thickness of the WS_2 layer increases, the friction coefficient first increases and then decreases, which is lower than that of the monolithic high-entropy (AlCrTiZrNb)N film. The microstructural evolution is the main reason for the variation of friction coefficients.

CRediT authorship contribution statement

PC and WL designed the experiment and wrote the article. PL and KZ carried out the synthesis of films. JW, XM, FM, XC, RF and PKL assisted the technical support for measurements as well as the data analysis. All authors read and approved the final manuscript.

Declaration of competing interest

The authors declare that they have no known competing financial interests or personal relationships that could have appeared to influence the work reported in this paper.

Acknowledgment

The present work was financially supported by the National Natural Science Foundation of China (No. 51971148, 51471110). P.K.L. very much appreciates the supports from the National Science Foundation (DMR-1611180 and 1809640) with program directors, Drs. J. Yang, G. Shiflet, and D. Farkas.

References

[1] S. Varalakshmi, M. Kamaraj, B.S. Murty, Processing and properties of nanocrystalline CuNiCoZnAlTi high entropy alloys by mechanical alloying, Mater. Sci. Eng. A 527 (2010) 1027–1030.
[2] P.F. Yu, L.J. Zhang, H. Cheng, H. Zhang, M.Z. Ma, Y.C. Li, G. Li, P.K. Liaw, R.P. Liu, The high-entropy alloys with high hardness and soft magnetic property prepared by mechanical alloying and high-pressure sintering, Intermetallics 70 (2016) 82–87.
[3] W. Li, P. Liu, P.K. Liaw, Microstructures and properties of high-entropy alloy films and coatings: a review, Mater. Res. Lett. 6 (2018) 199–229.
[4] Y.C. Liu, Y.H. Cho, Elucidating the microstructural and tribological characteristics of NiCrAlCoCu and NiCrAlCoMo multicomponent alloy clad layers synthesized in situ, Surf. Coat. Technol. 203 (2009) 1694–1701.
[5] M.H. Chuang, M.H. Tsai, W.R. Wang, S.J. Lin, J.W. Yeh, Microstructure and wear behavior of $Al_xCo_{1.5}CrFeNi_{1.5}Ti_y$ high-entropy alloys, Acta Mater. 59 (2011) 6308–6317.
[6] M. Chen, X.H. Shi, H.J. Yang, P.K. Liaw, M.C. Gao, J.A. Hawk, J.W. Qiao, Wear behavior of $Al_{0.6}$CoCrFeNi high-entropy alloys: effect of environments, J. Mater. Res. 33 (2018) 3310–3320.
[7] M.A. Hemphill, T. Yuan, G.Y. Wang, J.W. Yeh, C.W. Tsai, A. Chuang, P.K. Liaw, Fatigue behavior of $Al_{0.5}$CoCrCuFeNi high entropy alloys, Acta Mater. 60 (2012) 5723–5734.
[8] Z. Tang, T. Yuan, C.W. Tsai, J.W. Yeh, C.D. Lundin, P.K. Liaw, Fatigue behavior of a wrought $Al_{0.5}$CoCrCuFeNi two-phase high-entropy alloy, Acta Mater. 99 (2015) 247–258.
[9] S. Shukla, T.H. Wang, S. Cotton, R.S. Mishra, Hierarchical microstructure for improved fatigue properties in a eutectic high entropy alloy, Scr. Mater. 156 (2018) 105–109.
[10] K.V.S. Thurston, B. Gludovatz, Q. Yu, G. Laplanche, E.P. George, R.O. Ritchie, Temperature and load-ratio dependent fatigue-crack growth in the CrMnFeCoNi high-entropy alloy, J. Alloys Compd. 794 (2019) 525–533.
[11] M. Seifi, D. Li, Z. Yong, P.K. Liaw, J.J. Lewandowski, Fracture toughness and fatigue crack growth behavior of as-cast high-entropy alloys, JOM (2015) 2288–2295.
[12] C.P. Lee, C.C. Chang, Y.Y. Chen, J.W. Yeh, H.C. Shih, Effect of the aluminium content of $Al_xCrFe_{1.5}MnNi_{0.5}$ high-entropy alloys on the corrosion behaviour in aqueous environments, Corros. Sci. 50 (2008) 2053–2060.
[13] Y.Z. Shi, L. Collins, N. Balke, P.K. Liaw, B. Yang, In-situ electrochemical-AFM study of localized corrosion of Al_xCoCrFeNi high-entropy alloys in chloride solution, Appl. Surf. Sci. 439 (2018) 533–544.
[14] Y.Z. Shi, L. Collins, R. Feng, C. Zhang, N. Balke, P.K. Liaw, B. Yang, Homogenization of Al_xCoCrFeNi high-entropy alloys with improved corrosion resistance, Corros. Sci. 133 (2018) 120–131.
[15] Y.Z. Shi, B. Yang, X. Xie, J. Brechtl, K.A. Dahmen, P.K. Liaw, Corrosion of Al_xCoCrFeNi high-entropy alloys: Al-content and potential scan-rate dependent pitting behavior, Corros. Sci. 119 (2017) 33–45.
[16] Y.Z. Shi, B. Yang, P.K. Liaw, Corrosion-resistant high-entropy alloys: a review, Metals. 7 (2017) 43.
[17] J.W. Yeh, S.K. Chen, S.J. Lin, J.Y. Gan, T.S. Chin, T.T. Shun, C.H. Tsau, S.Y. Chang, Nanostructured high-entropy alloys with multiple principal elements: novel alloy design concepts and outcomes, Adv. Eng. Mater. 6 (2004) 299–303.
[18] B. Cantor, I.T.H. Chang, P. Knight, A.J.B. Vincent, Microstructural development in equiatomic multicomponent alloys, Mater. Sci. Eng. A 375-377 (2004) 213–218.
[19] Y. Zhang, T.T. Zuo, Z. Tang, M.C. Gao, K.A. Dahmen, P.K. Liaw, Z.P. Lu, Microstructures and properties of high-entropy alloys, Prog. Mater. Sci. 61 (2014) 1–93.
[20] D.B. Miracle, O.N. Senkov, A critical review of high entropy alloys and related concepts, Acta Mater. 122 (2017) 448–511.
[21] J.M. Wu, S.J. Lin, J.W. Yeh, S.K. Chen, Y.S. Huang, H.C. Chen, Adhesive wear behavior of Al_xCoCrCuFeNi high-entropy alloys as a function of aluminum content, Wear 261 (2006) 513–519.
[22] W.H. Liu, Y. Wu, J.Y. He, T.G. Nieh, Z.P. Lu, Grain growth and the Hall–Petch relationship in a high-entropy FeCrNiCoMn alloy, Scr. Mater. 68 (2013) 526–529.
[23] M.A. Hemphill, T. Yuan, G.Y. Wang, J.W. Yeh, C.W. Tsai, A. Chuang, P.K. Liaw, Fatigue behavior of $Al_{0.5}$CoCrCuFeNi high entropy alloys, Acta Mater. 60 (2012) 5723–5734.
[24] B. Cantor, Multicomponent high-entropy Cantor alloys, Prog. Mater. Sci. 120 (2020) 100754.
[25] Y.J. Zhou, Y. Zhang, F.J. Wang, G.L. Chen, Phase transformation induced by lattice distortion in multiprincipal component CoCrFeNiCuxAl_{1-x} solid-solution alloys, Appl. Phys. Lett. 92 (2008) 299.
[26] C.J. Tong, Y.L. Chen, J.W. Yeh, S.J. Lin, S.K. Chen, T.T. Shun, C.H. Tsau, S. Y. Chang, Microstructure characterization of Al_xCoCrCuFeNi high-entropy alloy system with multiprincipal elements, Metall. Mater. Trans. A 36 (2005) 881–893.
[27] C.L. Tracy, Park Sulgiye, D.R. Rittman, S.J. Zinkle, H. Bei, Maik Lang, R.C. Ewing, Wendy L. Mao, Formation of a hexagonal close-packed phase of the high-entropy alloy CrMnFeCoNi at high pressure, Nat. Commun. 8 (2016) 15634.
[28] Y.P. Lu, X.Z. Gao, L. Jiang, Z.N. Chen, T.M. Wang, J.C. Jie, H.J. Kang, Y.B. Zhang, S. Guo, H.H. Ruan, Y.H. Zhao, Z.Q. Cao, T.J. Li, Directly cast bulk eutectic and near-eutectic high entropy alloys with balanced strength and ductility in a wide temperature range, Acta Mater. 124 (2017) 143–150.
[29] Y.P. Lu, Y. Dong, S. Guo, L. Jiang, H.J. Kang, T.M. Wang, B. Wen, Z.J. Wang, J. C. Jie, Z.Q. Cao, H.H. Ruan, Y.H. Zhao, T.J. Li, A Promising new class of high-temperature alloys: eutectic high-entropy alloys, Sci. Rep. 4 (2014) 6200.
[30] Y.P. Lu, Y. Dong, H. Jiang, Z.Q. Cao, S. Guo, T.M. Wang, Peter K. Liaw, Promising properties and future trend of eutectic high entropy alloys, Scr. Mater. 187 (2020) 202–209.
[31] T.H. Hsieh, C.H. Hsu, C.Y. Wu, J.Y. Kao, C.Y. Hsu, Effects of deposition parameters on the structure and mechanical properties of high-entropy alloy nitride films, Curr. Appl. Phys. 18 (2018) 512–518.
[32] J.S. Koehler, Attempt to design a strong solid, Phys. Rev. B 2 (1970) 547–551.
[33] G.J. Zhang, T. Wang, H.L. Chen, Microstructure, mechanical and tribological properties of TiN/Mo_2N nano-multilayer films deposited by magnetron sputtering, Surf. Coat. Technol. 61 (2015) 156–160.
[34] W.C. Oliver, G.M. Pharr, An improved technique for determining hardness and elastic modulus using load and displacement sensing indentation experiments, J. Mater. Res. 7 (1992) 1564–1583.
[35] J.Y. Li, J.H. Xu, L.Q. Zhang, L. Wu, M.Y. Gu, Growth, microstructure, and microhardness of W/Mo nanostructured multilayers, J. Vac. Sci. Technol. B 19 (2001) 94–97.

[36] U. Helmersson, S. Todorona, S.A. Barnett, J.E. Sundgren, L.C. Markert, J.E. Greene, Growth of single-crystal TiN/VN strained-lay superlattice with extremely high mechanical hardness, J. Appl. Phys. 62 (1987) 481–484.
[37] P.B. Mirkarlmi, L. Hultman, S.A. Barnett, Enhanced hardness in lattice-matched single-crystal TiN/$V_{0.6}Nb_{0.4}N$ superlattices, J. Appl. Phys. Lett. 57 (1990) 2654–2656.
[38] T.I. Selinder, M.E. Sjostraned, M. Nordin, Mats Larsson, A. Ostlund, Sture Hogmark, Performance of PVD TiN/TaN and TiN/NbN superlattice coated cemented carbide tools in stainless steel machining, Surf. Coat. Technol. 105 (1998) 51–55.
[39] G.Y. Li, Z.H. Han, J.W. Tian, J.H. X, M.Y. Gu, Alternating stress field and superhardness effect in TiN/NbN superlattice films, J. Vac. Sci. Technol. A 20 (2002) 674–677.
[40] P. Yashar, X. Chu, S.A. Barnett, J. Rechner, W.D. Sproul, Stabilization of $CrN_{0.6}$ in $CrN_{0.6}$/TiN superlattices, Appl. Phys. Lett. 72 (1998) 987–989.
[41] M. Kato, T. Mori, L.H. Schwartz, Hardening by spinodal modulated structure, Acta Metall. 28 (1980) 285–290.